International Journal of Modern Physics C
Vol. 33, No. 7 (2022) 2250090 (17 pages)

DOI: 10.1142/S0129183122500905

Properties of the compressibility and transport motion in wall-bounded turbulent flows at Mach 8

Xin Li*, Siyuan Zhang†,¶, Junyi Duan‡,§, Xiaobo Liu* and Wanghao Wu*

*Shanghai Electromechanical Engineering Institute
Shanghai 201109, P. R. China

†School of Mechanical Engineering
University of Shanghai for Science and Technology
Shanghai 200093, P. R. China

‡LHD, Institute of Mechanics
Chinese Academy of Sciences, Beijing 100190, P. R. China

§School of Engineering Science
University of Chinese Academy of Sciences
Beijing 100049, P. R. China
¶zhangsiyuan@usst.edu.cn

Received 28 October 2021
Accepted 2 December 2021
Published 6 January 2022

The compressibility effect and transport motion in highspeed turbulent boundary layer (TBL) is a fundamental problem because they dominate the average and statistical characteristics. Using the statistical methods and flow visualization technology, flat-plate TBLs at $Ma_\infty = 8$ with high- and low-wall temperatures, $T_w/T_\infty = 10.03$ and 1.9, are investigated based on the direct numerical simulation (DNS) datasets. Compared with previous studies, this study considers relative higher Mach number and strong cold wall temperature condition at the same time. First, the turbulent Mach number and turbulent intensity show that the compressibility effects are enhanced by the cooling process. Second, the high-order statistical moments and structure parameters confirm cold wall that causes stronger compressibility and the corresponding increased intensities of local streamwise and wall-normal transport motions. Finally, for uncovering the relationship between the compressibility effect and turbulent transport, more in-depth visualization analyses of velocity streaks are performed. It is found that 'knot-like' structures are generated when cooling the wall, and they lead to stronger intermittent, which results in the rapid increase of local compressibility effect and the wall-normal transport motion. Our research sheds light on providing a theoretical basis for further understanding the compressibility effects of TBL at high Mach number.

Keywords: Direct numerical simulation; turbulent boundary layer; wall temperature effect; high Mach number.

PACS Nos.: 47.40.−x, 47.53.+n.

¶Corresponding author.

1. Introduction

With a great increasing flight speed, the aerodynamic and thermal problems caused by the turbulent boundary layer (TBL) on aircraft surface become prominent sharply. Generally speaking, these problems are closely related to the compressibility and transport motion in TBL, whose features have not yet been predicted accurately.[1] At the same time, due to the effects of heat transfer and thermal radiation on aircraft surface, the compressibility and transport motion will be complicated by the obvious temperature difference. Therefore, it is necessary to investigate the effects of wall temperature on compressibility and transport motion in depth at high Mach number.

Direct numerical simulation (DNS) is an important method for investigating turbulent mechanisms. Limited by computing technology, most of the previous DNS studies with wall temperature effects focus on supersonic condition. Guo and Adams[2] take the lead in temporal DNS of compressible flat-plate TBL, revealing that the compressibility has little effect on the expansion dissipation term and pressure expansion term of turbulent kinetic energy with hot wall conditions at $Ma_\infty = 3$, 4.5 and 6. Subsequently, Guarini[3] studies adiabatic flat-plate TBL at $Ma_\infty = 2.5$ to confirm the similar statistical features to those of incompressible turbulence. To spread the spatial simulation range, Rai *et al.*[4] perform spatially DNS to simulate TBL at $Ma_\infty = 2.25$ and point out that the mean velocity, first- and second-order statistics under Van driest transform[5] are consistent with the incompressible turbulence under supersonic condition. Pirozzoli *et al.*[6] and Gao *et al.*[7] use higher precision numerical methods and more dense grids to obtain clearer statistical characteristics and also visualize the flow fields. Although the studies obtained great progress in TBL, but the results have not been applicable enough to high Mach conditions.

Gradually, DNS is applied to the TBL at higher Mach numbers. Maeder *et al.*[8] simulate the flat-plate TBL at $Ma_\infty = 3 \sim 6$. Their results show that when the Mach number is less than 5, the compressibility effect can be ignored. At this time, Morkovin's hypothesis is still valid. Li *et al.*[9] find mainly quasi-streamwise vortices and little hairpin vortices in flat-plate TBL at $Ma_\infty = 6$, which are very different from the low Mach number cases. Duan and Martín[10–12] systematically study the wall temperature effect, Mach number effect and high enthalpy effect on compressible TBLs, of which the highest freestream Mach number is $Ma_\infty = 12$. They point out that when close to the adiabatic wall temperature, the compressibility effect is not obvious in the main statistical features such as mean velocity, mean temperature and turbulence intensity, while the van Driest transformed velocity is in good agreement with incompressible turbulence, and the mean temperature collapses to Walz's equation or Crocco's relation.[13] The density-scaling turbulence intensity is similar to that of incompressible flows. The production, dissipation and transport distribution of turbulent energy at different Mach numbers are also in good agreement with the measurement of semi-local coordinates.[14] The results indicate that when the wall temperature is close to the adiabatic wall, Morkovin's hypothesis is still partially effective at Ma_∞ up to 12. Lagha *et al.*[15,16] extend the DNS range to

$Ma_\infty = 20$ to study the influence of compressibility on turbulence statistics and coherent structures. Liang and Li[17,18] use DNS to study the flat-plate turbulence for wide range of $Ma_\infty = 2.25 - 8$. The high wall temperature approximates the recovery temperature and the lower one only 0.2 times the recovery temperature. They develop a modified strong Reynolds analogy for high Mach number and strong cold wall temperature. Duan *et al.*[19,20] conduct systematic analyses of the statistical characteristics of the pressure field for a cold-wall flat-plate boundary layer at $Ma_\infty = 6$. They found that the cooled wall has the most significant effect on the nonlinear component of the sound source term. Later, authors also focused on the Reynolds stress and coherent structures at $Ma_\infty = 8$.[21,22]

From the above literature, it can be observed that the previous studies mainly focus on the classical mean quantities and low-order statistics to describe the basic properties of the turbulence. The corresponding essential mechanism reflected by the coherent structure is still not so clear, which is the most important in connecting and uncovering compressibility effect and transfer motion. Besides, DNS study of the wall temperature effect over TBL at high Mach number is limited. It is very necessary to carry out DNS study in this field. For the purpose of this study, DNS databases over flat-plate TBLs at $Ma_\infty = 8$ with two different wall temperatures conditions are used to study the effects of wall temperature on compressibility and transport motion.[17,18]

This paper is structured as follows. Governing equations and computation setup are given in Sec. 2. Turbulence statistics and flow visualization technology are given in Sec. 3. Finally, conclusions are drawn in Sec. 4.

2. Governing Equations and Computation Setup for DNS

The governing equations solved in this paper for DNS are nondimensional continuity, momentum and energy equations in conservative form on the Cartesian coordinate system (See Eq. (1)). The flow parameters ρ, u, v, w, T, p need to be nondimensionalized by the characteristic quantities ρ_∞, U_∞, U_∞, U_∞, T_∞ and $\rho_\infty U_\infty^2$, respectively, where the subscript ∞ represents the free stream. The characteristic length L to nondimensionalize the length scale is a length unit as inch. The characteristic viscosity coefficient and heat conductivity coefficient are μ_∞ and κ_∞.

$$\frac{\partial U}{\partial t} + \frac{\partial (F - F_v)}{\partial x} + \frac{\partial (G - G_v)}{\partial y} + \frac{\partial (H - H_v)}{\partial z} = 0, \tag{1}$$

where U represents the conservative variables, F, G, H and F_v, G_v, H_v represent the numerical inviscid and viscous flux functions, respectively.

The specific form of conserved variables is as follows:

$$U = \begin{pmatrix} \rho \\ \rho u \\ \rho v \\ \rho w \\ \rho e_t \end{pmatrix}, \tag{2}$$

where ρ denotes the density of the fluid. u, v and w are the velocities in the x, y and z directions, respectively. $e_t = c_v T + 1/2(u^2 + v^2 + w^2) = \frac{p}{(\gamma-1)}\rho + 1/2(u^2 + v^2 + w^2)$ is the total energy of per unit mass, where T is the temperature and c_v is the constant specific heat capacity.

The specific forms of inviscid fluxes are given by

$$F = \begin{pmatrix} \rho u \\ \rho uu + p \\ \rho uv \\ \rho uw \\ (\rho e_t + p)u \end{pmatrix}, \quad G = \begin{pmatrix} \rho v \\ \rho vu \\ \rho vv + p \\ \rho vw \\ (\rho e_t + p)v \end{pmatrix}, \quad H = \begin{pmatrix} \rho w \\ \rho wu \\ \rho wv \\ \rho ww + p \\ (\rho e_t + p)u \end{pmatrix}, \tag{3}$$

and viscous fluxes can be expressed as follows:

$$F_v = \begin{pmatrix} 0 \\ \tau_{xx} \\ \tau_{xy} \\ \tau_{xz} \\ \Theta_x \end{pmatrix}, \quad G_v = \begin{pmatrix} 0 \\ \tau_{yx} \\ \tau_{yy} \\ \tau_{yz} \\ \Theta_y \end{pmatrix}, \; H_v = \begin{pmatrix} 0 \\ \tau_{zx} \\ \tau_{zy} \\ \tau_{zz} \\ \Theta_z \end{pmatrix}. \tag{4}$$

Here, from symmetry, the stress can be written as follows:

$$\begin{aligned} \tau_{xy} &= \tau_{yx} = \mu\left(\frac{\partial u}{\partial y} + \frac{\partial v}{\partial x}\right) \\ \tau_{xz} &= \tau_{zx} = \mu\left(\frac{\partial u}{\partial z} + \frac{\partial w}{\partial x}\right), \\ \tau_{zy} &= \tau_{yz} = \mu\left(\frac{\partial v}{\partial z} + \frac{\partial w}{\partial y}\right) \end{aligned} \tag{5}$$

where the dynamic viscosity coefficient μ obtained by Sutherland's formula is as follows:

$$\mu = \frac{1}{Re_\infty} \frac{T^{\frac{3}{2}}(1 + T_s/T_\infty)}{T + T_s/T_\infty}. \tag{6}$$

where $Re_\infty = \rho_\infty U_\infty L/\mu_\infty$ representing the free-stream Reynolds number, and, $T_s = 110.4\,\mathrm{K}$ representing the reference temperature parameter.

According to energy transform and Fourier's law, we define

$$\begin{aligned} \Theta_x &= u\tau_{xx} + v\tau_{xy} + w\tau_{xz} + k\frac{\partial T}{\partial x} \\ \Theta_y &= u\tau_{xy} + v\tau_{yy} + w\tau_{yz} + k\frac{\partial T}{\partial y}, \\ \Theta_z &= u\tau_{xz} + v\tau_{yz} + w\tau_{zz} + k\frac{\partial T}{\partial z} \end{aligned} \tag{7}$$

where k is the mixture heat conductivity.

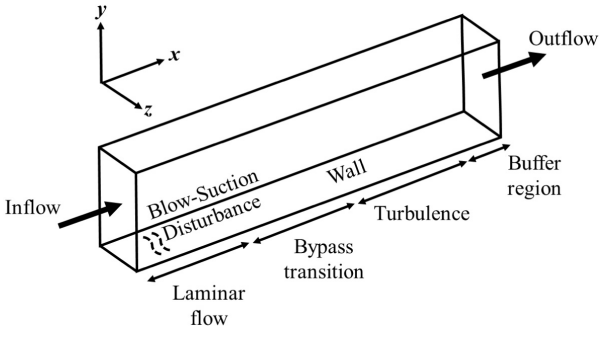

Fig. 1. Sketch of computational domain and coordinate system for the flat-plate flows, including laminar, transitional and turbulent regions.

As shown in Fig. 1, x, y, z denote free-stream, wall-normal and spanwise directions, respectively. Along the streamwise direction, the computational domain successively includes laminar, transitional and turbulent regions. The inflow conditions come from the computation of two-dimensional laminar flat-plate flows. The parameter profiles at a streamwise position are copied along spanwise direction for three-dimensional computation. Near the inflow plane, blow-suction disturbance is set on the wall to promote the bypass transition process. No-slip and isothermal conditions are applied. In order to inhibit the reflection of the numerical disturbance, the progressively coarsening meshes are generated near the upper far field and outlet boundary. For spanwise direction, periodic boundary conditions are used on the computational domain.

The flow conditions are shown in Table 1, where TH and TL denote the high and low isothermal wall conditions, respectively.

Table 1 provides different definitions of Reynolds number at the selected y-z planes, where $Re_{\delta 2} \equiv \rho_\delta u_\delta \theta / \mu_w$ and $Re_\theta \equiv \rho_\delta u_\delta \theta / \mu_\delta$ based on the momentum thickness θ, density, velocity at the edge of the boundary layer and viscosity at the wall and edge of the TBL. We use δ to denote the nominal thickness.

As shown in Table 2, L_x, L_y and L_z denote the length of computational domain in the streamwise, wall-normal and spanwise directions. $N_x \times N_y \times N_z$ indicates the corresponding number grid points. The grid is equally spaced in the spanwise direction. In order to capture the fine turbulent structures, the uniformly spaced and finest grids are employed in turbulent region in streamwise direction. For reducing the computation cost, relative sparse grids and transitional grids are used in laminar and transition regions, respectively. Along with the wall-normal direction, an

Table 1. Flow conditions for the flat-plate DNS.

Case	Ma_∞	T_∞ (K)	T_w/T_∞	T_w/T_r	$Re_{\delta 2}$	Re_θ	δ
TH	8	169.44	10.03	0.80	6328.23	3.71×10^4	0.25
TL	8	169.44	1.90	0.15	6763.45	1.24×10^4	0.12

Table 2. Computational domains and grid parameters for the DNS.

Case	$L_x \times L_y \times L_z$	$N_x \times N_y \times N_z$	$dx^+ \times dy^+ \times dz^+$
TH	$37 \times 0.7 \times 0.3$	$12460 \times 100 \times 320$	$12.2 \times 0.96 \times 4.6$
TL	$11 \times 7 \times 0.18$	$8950 \times 90 \times 640$	$11.2 \times 1.0 \times 4.5$

exponential grid distribution is adopted. The first point near by the wall locates at about one viscous length scale. The grid resolutions based on the viscous scale are comparable with previous DNS cases.[6,10,23]

In the DNS, the numerical method combines the WENO-JS7 scheme for the inviscid fluxes and the eighth-order central difference for the viscous terms. Comparing with other improved low-dissipation scheme, even though the present WENO scheme may be dissipative, the enough dense grids are considered to eliminate the impact of dissipation. The time-advancement is evaluated using the explicit third-order accurate Runge–Kutta method.

For the selected streamwise direction in the subsequent analysis, both cases are fully developed turbulence. For converged statistical analysis, the selected y-z planes contain 1100 and 1800 sections for TH and TL cases, respectively. The corresponding interval time spacing is $0.02\delta/U_\infty$ and $0.04\delta/U_\infty$, and the span of time is $22\delta/U_\infty$ and $72\delta/U_\infty$. The data average contains both time and spanwise averages.

The DNS is parallelly computed on Tianhe-1, National Super Computer Center in Tianjin by 9216 CPUs about 152 system hours. The supercomputing node used is configured as a two-way 12 cores, ($2 *$ lntel Xeon $\times$ 5670 @ 2.93GHz, 24GB RAM). Since the nodes are only used for this task, the CPU time is close to the system time. The self-developed OpenCFD software contains reasonable allocation of public and private variables, which not only ensures enough public variables throughout the whole calculation process, but also needs enough private variables to release the memory. Before parallel computing, it is necessary to allocate CPU numbers in three directions of the computing domain to maintain load balance as much as possible to improve the computing speed. In parallel computing, MPI blocking communication method is used to package the edge data of each parallel sub-block and then send it to adjacent sub- blocks. Through the above optimization methods, large-scale parallel computing can be carried out smoothly.

3. DNS Data and Analysis

Details regarding the accuracy of the DNS statistics as compared to other many DNS datasets and experiments are provided in Liang.[17,18]

Turbulent Mach number $M_t = \sqrt{\overline{u'^2 + v'^2 + w'^2}}/\bar{c}$ is an important indicator for measuring the compressibility effect of TBL, where $\bar{c} = \sqrt{\gamma R\bar{T}} = \sqrt{\bar{T}}/Ma_\infty$ is the local mean sound speed. Figure 2 compares the current DNS results with Duan's adiabatic condition at $Ma_\infty = 5$. For each case, the magnitude of M_t increases first

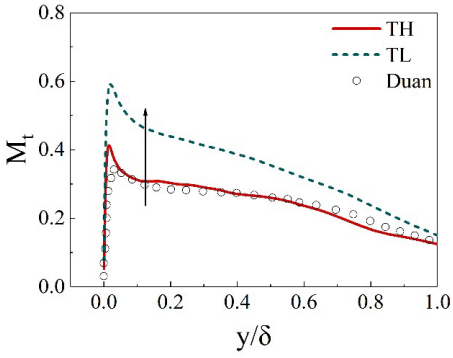

Fig. 2. Turbulence Mach number M_t for present results and Duan's adiabatic result with $Ma_\infty = 5$.[10]

and then decreases. M_t for the TH case and Duan's agree well except that it is increasing slightly at the peak. It is because the wall temperatures of both cares are close to the adiabatic condition, so the flow features are very similar. Through the whole boundary layer, the magnitude of M_t increases significantly, and the peak value increased from 0.41 to 0.6, but the change trend is still consistent with the TH case. At the same wall-normal location, we note that the amplitude enhancement of M_t near the wall is greater than that of the far wall, indicating the influenced range of wall temperature is only in the near-wall region. The increased compressibility effect can be corroborated from the side by the probability distribution functions for the density and velocity as shown in authors' previous studies.[21,24] The above results further verify that the cooled wall enhances the compressibility effect of TBL.

The root mean square (RMS) of velocity fluctuation, defined as $u'_{\rm rms} = \sqrt{u'^2}$, is used to characterize the turbulence intensity. The distribution of RMS of velocity along the wall-normal direction of the wall is shown in Fig. 3. The nominal boundary layer thickness δ is used to nondimensionalize the wall-normal distance, and the wall friction velocity u_τ is used to normalized RMS. It can be seen that the turbulence intensities in the three directions increase from the wall rapidly and reaches the peak value soon, especially the streamwise velocity fluctuation. Then, the turbulence intensity decreases gradually as it approaches the boundary-layer edge. When cooling the wall, the turbulence intensity is enhanced significantly up to approximately two times the TL case. The results show that reducing the wall temperature enhances the overall turbulence intensity.

From the study of incompressible flow, the 'structure parameter' is defined as $-u'v'/2k$, whose value is approximately constant between 0.14 and 0.17.[23] Figure 4 plots $-u'v'/2k$ for both DNS cases. It is shown that $-u'v'/2k$ increases along the wall-normal direction, but they are approximately constant at $y/\delta = 0.1$ for TH and 0.2 for TL cases, respectively. Smits *et al.*[25] consider that the structure parameter might change due to the effects of Reynolds number rather than Mach number. However, it can be observed that the relative position of the structure parameters for both cases is also impacted by the wall temperature at high Mach number, which

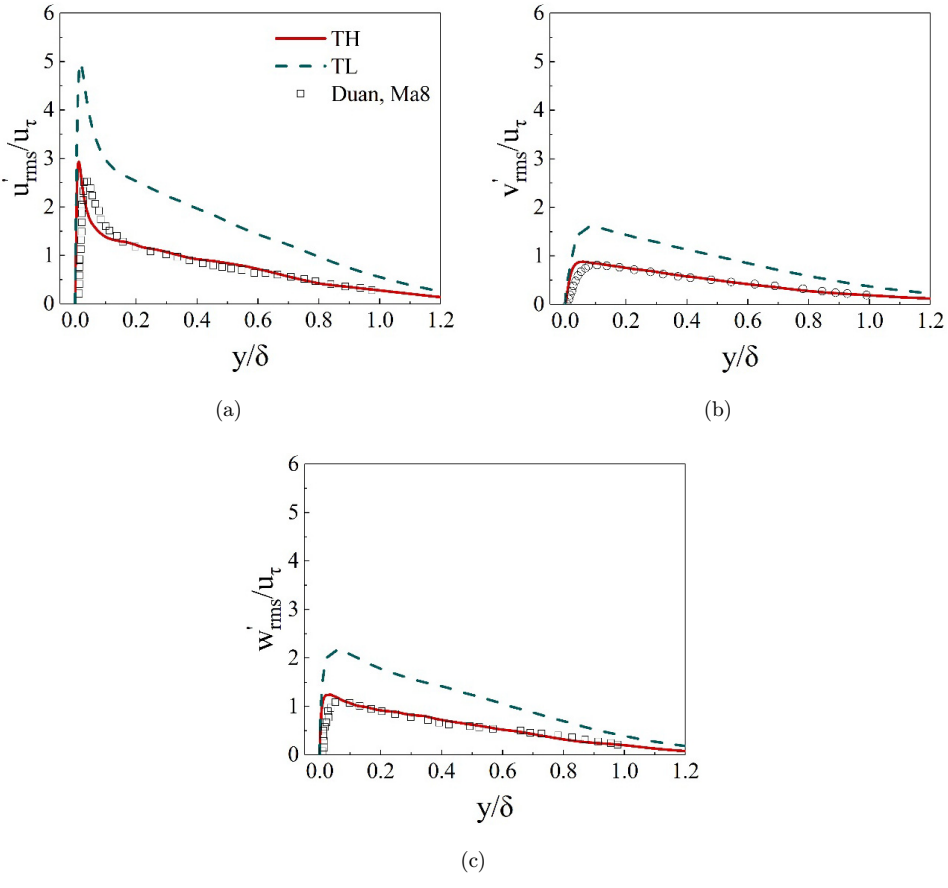

Fig. 3. Profiles of turbulence intensities of three velocity fluctuation components. (a) Streamwise velocity fluctuations u'; (b) Wall-normal velocity fluctuations v' and (c) Spanwise velocity fluctuations w'.

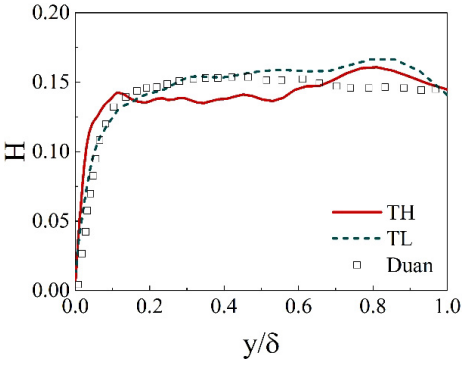

Fig. 4. Structure parameter $-u'v'/2k$ for TH and TL cases.[11,12]

indicates that the cooled wall enhances the anisotropy as the compressibility increases. The structure parameter also represents the compressibility effect on the wall-normal velocity fluctuation. It shows that although the wall-normal transport is weaker than that on the streamwise transport when cooling the wall, the Reynolds shear stress still maintain 15% in the whole transport motion. The result is a supplement to the results of Mach 3–12 under adiabatic wall condition.

Figure 5 plots the high-order (first- to fourth-order) moments $\bar{u}^n/U_\tau^n$ scaled by density for TH and TL cases, comparing with Duan's result under adiabatic wall.[26] Fig. 5(a) shows that the RMS of density-scaling velocity for both DNS cases is significantly closer than Fig. 3(a), but they do not completely coincide. The curves for TH and TL cases reach peaks at $y^+ = 20$ and $y^+ = 40$, respectively, representing the location of active local turbulent motion. The peak value and wall-normal position for TL case are larger than the TH case, which may come from the superposition effect of outer large-scale motion on the near-wall small-scaled motion. For the TH case, the results coincide with Schlatter's result only except for the peak value,

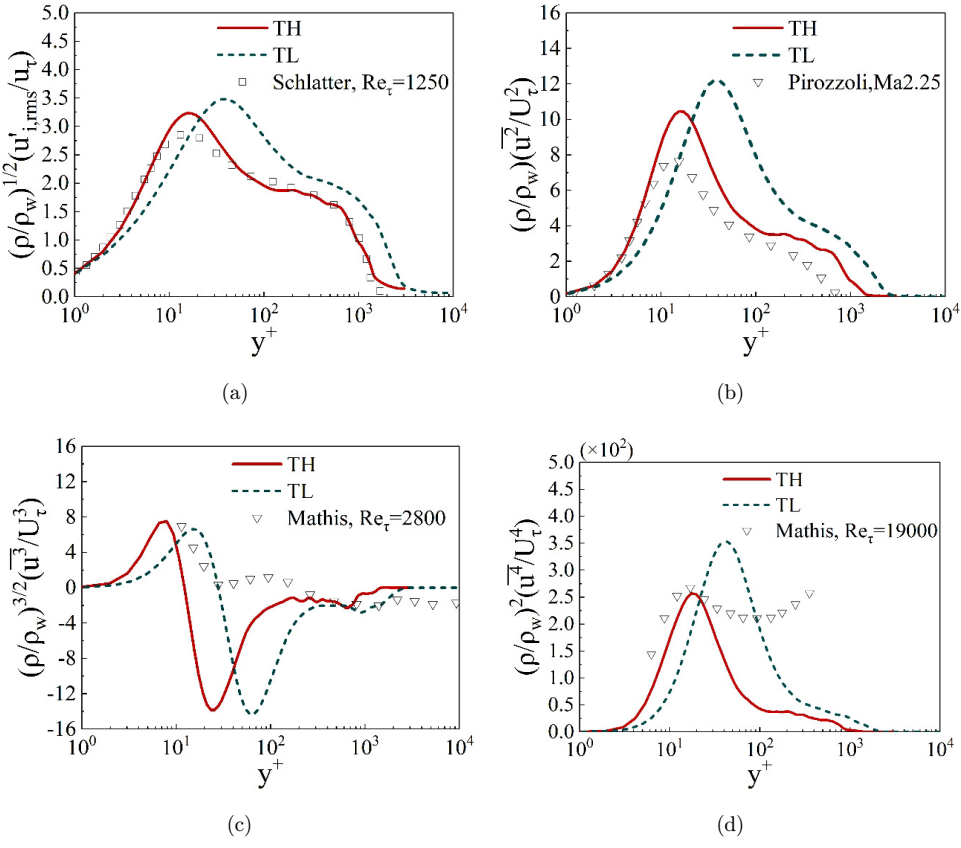

Fig. 5. Profiles of density-weighted turbulent high order statistics for TH and TL cases. (a) $n = 1$, (b) $n = 2$, (c) $n = 3$ and (d) $n = 4$.

indicating Morkovin's hypothesis is still partially applicable for nearly the adiabatic temperature, but there exists a large offset when the wall temperature is cold enough. The second-order moments are plotted in Fig. 5(b). Since the second-order moments are the square of RMS, they have similar features to Fig. 5(a). However, it can be seen that the deviation of the second-order moments between the results for TH and TL cases further increases, and the peak increase caused by the increase of Mach number is more obvious. The TH case has increased about twice in comparison with $Ma_\infty = 2.25$, and the adiabatic wall is no longer a sufficient condition for uniformly scaling the velocity fluctuation.[6] Figure 5(c) provides a comparison between the third-order moments at high Mach number and the results of incompressible turbulence. Compared with the first- and second-order moments, the third-order moments exhibit negative values which is qualitatively consistent with the result of the incompressible flow. But at the similar magnitude of Re_τ, the absolute peak value of strong compressible flow is much larger than that of incompressible flow, and tends to be negative, indicating that the local intermittent and convective effects at high Mach number are greatly enhanced. Figure 5(d) represents the fourth-order moments of velocity fluctuations. For better comparison, an incompressible result with a very high Reynolds number $Re_\tau = 19\,000$ is selected here as a reference. It can be seen that the result of high Mach number compressible flow coincides well with the high Reynolds number incompressible flow near the wall, but there is a great difference away from the wall. This is because the large-scale motion in the outer layer is very active with high Reynolds number resulting in the appearance of the outer peak of fluctuations. The outer peak in the high-order moments appears earlier than that in the low-order moments. From the two high-order moments figures (Figs. 5(c) and 5(d)), we observe that in the fluctuation statistical moments, the influence of high Mach number can be certain equivalent to that of high Reynolds number. However, in the research range of this paper; no matter which order moments; the results for the TL case deviate from the TH case, while higher-order statistical moments are more sensitive to compressibility enhancement than those of lower order. This result implies that the heat-transfer effect of the strong cold wall invalidates the density measurement of higher-order moments of velocity fluctuations.

The expression of van Driest transformation is shown in Eq. (8).[5] Because wall friction velocity $u_\tau = \sqrt{\tau_w/\rho_w}$ contains wall density ρ_w, it is assumed that $\bar{\rho} = \rho_w$ in van Driest transformation. Figure 6(a) plots the distributions of van Driest mean streamwise velocities. The dotted line near the wall represents the linear law $y^+ = U^+$, and the inclined dotted line represents the log-law $U^+ = \frac{1}{\kappa} \ln y^+ + C$, here $\kappa = 41$, $C = 7.2$. It can be seen that through van Driest transformation, the slopes of the mean velocity profiles of both cases in the log-law region are in good agreement with the semi-theoretical value. It shows that the buffer region for the TL case is wider than that of the TH case, and the lower limit of the log-law region moves far away from the wall, which coincides with Fig. 5. The result indicates that the reduction of wall temperature makes the average features of the boundary layer deviate from the Morkovin's hypothesis. For the linear law region, the difference

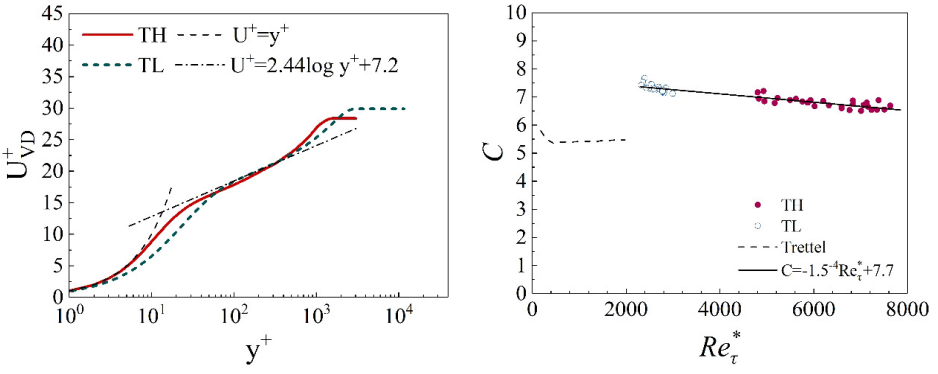

(a) (b)

Fig. 6. van Driest transformation and the intercept of the logarithm law of U^+_{VD} varies with Re^*_τ.

between both cases is evident because there is a strong heat transfer for the TL case which makes the wall scaling method partially invalid.

$$U^+_{\mathrm{VD}} = \int_0^{\bar{u}^+} \sqrt{\frac{\bar{\rho}}{\rho_w}} d\bar{u}^+. \tag{8}$$

Figure 6(b) plots the intercept of the van Driest transformed mean streamwise velocity vs Re^*_τ in the log-law region. Although van Driest transformation cannot completely unify the mean velocity profiles of different wall temperatures at high Mach numbers, their intercepts are still regular. The dotted line is the fitting curve of several compressible and incompressible TBLs in channel flows at $Ma_\infty \leq 4$ and relative low Reynolds numbers, they only occupy the left of the considered Reynolds region.[27] The results for the TH and TL cases are on the right. Because the computational domain of the TH case is longer than the TL case, the range of Reynolds number is wider. It can be seen that the distribution of the intercepts C for both cases are in a large range about 6.5–8, which is higher than the incompressible results. It also shows that the intercept of the TL case is generally higher than that of the TH case. This result is consistent with the distribution observed in the study.[18] At the same time, the intercepts for both cases are approximately distributed on a straight line with a negative slope, so the fitting straight line can be obtained by least-square fitting:

$$C = -1.5^{-4} Re^*_\tau + 7.7. \tag{9}$$

This fitting line provides a reference for the intercept prediction of the compressible TBL at high Mach numbers. This analysis also provides a positive effect in unifying the intercept of log-law by Re^*_τ.

Huang[14] proposes a semi-local nondimension wall scaling y^*, which is defined by Eq. (10). Compared with the classical y^+, the local flow information is taken into account for the wall scaling. Here, the mean velocity profiles are redrawn vs y^*, as

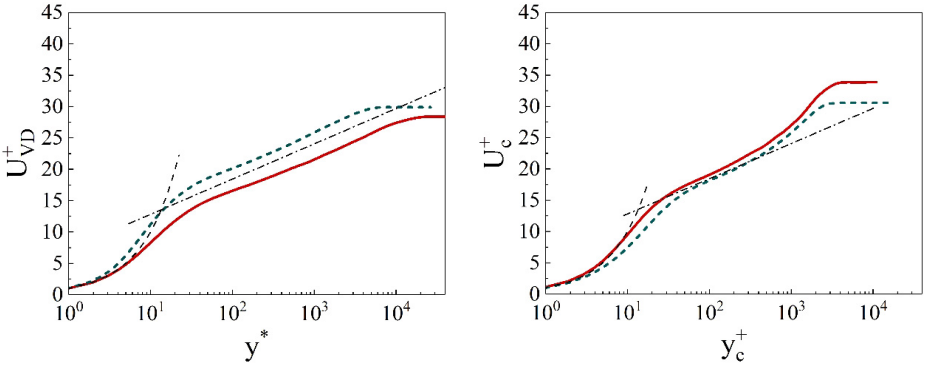

Fig. 7. The mean velocity profile on the y-z selected section. (a) van Driest transformation vs semi-local nondimension wall scale. (b) Improved van Driest transformation proposed by Brun.

shown in Fig. 7(a). It can be seen that the mean velocity profiles diverge from the wall law whether for the TH and TL cases, and then gradually separate away from the wall. In the log-law region, both curves always keep an approximatively constant distance and are on the different sides of the semi-theoretical predicted value. The above analyses clearly show that even considering the semi-logarithmic coordinates containing local flow quantities, the results under different temperatures cannot be measured uniformly, indicating the heat-transfer effect inducing by a strong cold wall has become very important for the local flow field.

$$y^* = \frac{\bar{\rho}(\tau_w/\bar{\rho})^{1/2}}{\bar{\mu}} y. \tag{10}$$

Subsequently, Brun *et al.*[28] improve the wall coordinate based on y^* and obtain y_c^+, see Eq. (11). They also propose an improved van Driest transformation that takes into account wall density, wall viscosity, local density and local viscosity (see Eq. (12)). Brun's numerical tests show that the transformation is suitable for a case with large temperature gradient on the wall at $Ma_\infty = 0.35$. It also can be seen from Fig. 7(b) that the results for the TH and TL cases in this paper become compact in the viscous sublayer and buffer layer, the gap of log-law only increases slightly, indicating that the local transport motions are active in very high Mach number and very low-wall temperature conditions.

$$y_c^+ = \int_0^{y^+} \left(\frac{\mu_w}{\bar{\mu}}\right) dy^+, \tag{11}$$

$$\bar{u}_c^+ = \int_0^{\bar{u}^+} \left(\frac{y^+}{y^{c+}}\right) \left(\frac{\mu_w}{\bar{\mu}}\right) \sqrt{\frac{\bar{\rho}}{\rho_w}} d\bar{u}^+. \tag{12}$$

In order to study the effect of near-wall heat-transfer on local turbulent transport, the instantaneous streamwise and wall-normal velocity fluctuations are further

analyzed. Here, the wall-normal height is at $y^+ \approx 15$, which is close to the maximum value of the production term in the turbulent kinetic energy equation. For comparing the results reasonably, all the contour bands are set to the same range. As shown in Figure 8(a) and 8(b), obvious streaks are extending along with the streamwise direction, and alternating positive and negative in the spanwise direction. It is considered that these streaks are the traces left by the quasi-streamwise vortex and hairpin vortex feet near the wall. Elongating along the streamwise direction does not mean a vortex structure has the same length as the streaks, but the overlapping multiple vortex structures lead to the formation of large-scale vortex packets. Therefore, the streamwise direction length of the vortex packet in the flows can be inferred from the length of the streaks. Consistent with the above, the length of

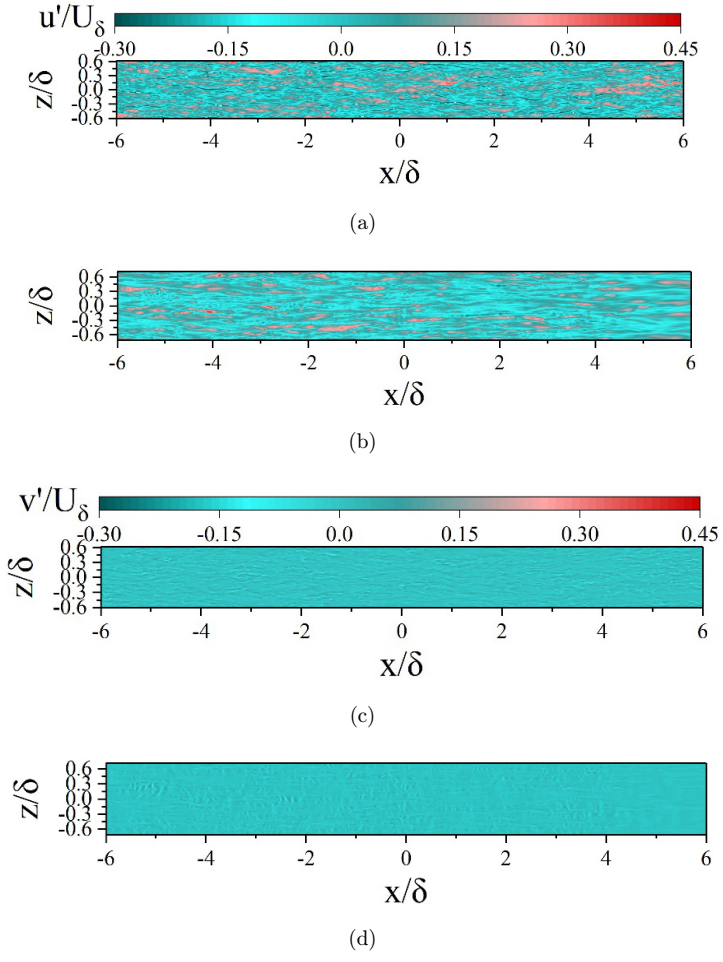

Fig. 8. Streamwise and wall-normal velocity fluctuation streaks. (a) u'/U_δ for TH case, (b) u'/U_δ for TL case, (c) v'/U_δ for TH case and (d) v'/U_δ for TL case.

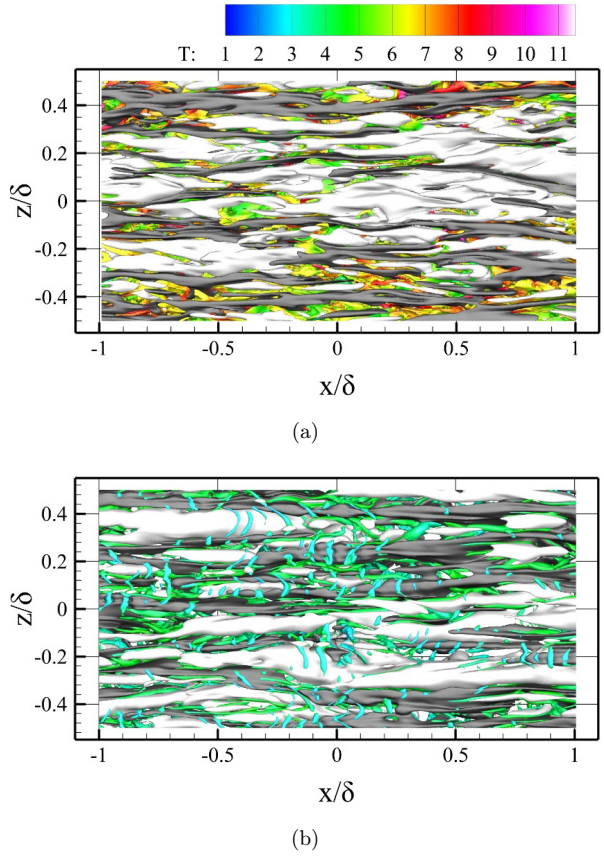

Fig. 9. Bottom views of coherent structures identified by $\Omega = 52$. Iso-surfaces of vortices are colored by local instantaneous temperature with the same color bars. Iso-surfaces of positive and negative streamwise velocity fluctuations are shown in white ($u'/u_\infty = 0.1$) and black ($u'/u_\infty = -0.1$), respectively. (a) TH case and (b) TL case.

streaks for the TH case is short and broken, while those for the TL case are longer and more organized.

As shown in Figs. 8(c) and 8(d), although the feature of the streaks of wall-normal velocity fluctuation is similar to that of the streamwise streaks, they are much dimmer than the latter, which indicates that the transport motions in the wall-normal direction are weaker than the stream-wise direction. However, it can be observed from the streaks of wall-normal velocity fluctuation for the TL case that some 'knot-like' structures exist seemingly randomly in the flow, this phenomenon has not been mentioned in the previous studies. These 'knot-like' structures are considered as strong intermittent local wall-normal transport motion which indicates the strong convection inducing by the heat transfer.

In order to validate the discussion and exhibit the 'knot-like' structures, Fig. 9 shows the bottom views of the three-dimensional vortex structures and the high and

low-momentum regions, that is, the part closest to the wall region. Here, the vortex structure is visualized by Ω criterion[29,30] and colored by the local average temperature in the same temperature range. The high- and low-momentum regions, represented by white and black, are defined by $u'/u_\infty = 0.1$ and -0.1, respectively. It can be seen that the high- and low-momentum regions represented are alternately arranged in the spanwise direction, confirming the 'knot-like' structure in Fig. 8. It is worth noting that for the TH case, the vortex structures are separate from in the high and low-momentum regions near the wall, and the near-wall regions are mainly dominated by the streamwise strip structures. However, for the TL case, the near-wall vortex structures present rich spanwise morphology, and some are highly distorted, winding around the high and low momentum region like a knot. In the previous heated wall simulation, the near-wall vortex structures are similar with the TH case.[31] But in the cooled wall simulation at Mach 5,[32] some statistical analyses show the increase in the distance of near-wall hairpin vortex legs. Later, recent studies about uniform-momentum zones and large-scale coherent structures find energetic frequencies product near the wall,[33,34] which also implies the slice views of the 'knot-like' structures in Fig. 8.

4. Conclusion

To conclude, in order to uncover the mechanism of the cooled-wall coherent structure, changing the turbulent statistics and transport motion over TBL at quite high Mach number ($Ma_\infty = 8$), we perform the statistical methods and flow visualization technology including turbulence Mach number, structure parameter, first- to fourth-order velocity fluctuation moments, transformed mean velocity and velocity streaks with high- and low-wall temperature conditions.

First, the DNS results of M_t and RMS show that the compressibility is strongly enhanced under cold wall condition whose magnitude is at least two times the TH case. The results are confirmed and analyzed. Second, to study the effect of compressibility on transport motion, the high-order statistical moments and structure parameters of streamwise velocity fluctuation are analyzed. The high-order moments show that the increase of compressibility caused by cold wall enhances local streamwise transport intensity and makes the position of the maximum value of transport intensity to move away from the wall. This phenomenon can be confirmed by the outward movement of the log-law region of the transformed mean velocity profile for the TL case. Higher-order statistical moments are more sensitive to compressibility enhancement than those of lower order. The compressibility effect on the wall-normal velocity fluctuation can be obtained from the structure parameter. This analysis shows that although the wall-normal transport is weaker than that on the streamwise transport when cooling the wall, the Reynolds shear stress still increases in the whole transport motion, reaching 15%. From the improved Van Driest transformation, it can be seen that the enhancement of the compressibility effect increases the local heat transfer. While introducing local heat transfer, the

transformed mean velocity profiles are more uniform. In this paper, the intercept is fitted by the least square method, and an empirical formula is obtained.

Finally, in order to further study the relationship between the compressibility effect and turbulent transport motion, visualization analyses of velocity streaks and vortex structures are carried out. The results show that the cold wall condition enhances the organization of the streamwise velocity fluctuation which indicates that the organization of the vortex structures is enhanced. Some 'knot-like' structures appear in the near-wall region, which show rich spanwise morphology and some of which are highly distorted. The 'knot-like' structures lead to stronger intermittent, then result in the rapid increase of local compressibility effect and the wall-normal transport motion in the wall-normal direction of the turbulence.

Acknowledgments

This work was supported by the NSFC Project (Grant No. U20B2007). The authors would like to thank Prof. Xinliang Li in LHD, Institute of Mechanics, Chinese Academy of Sciences for providing DNS database and the National Supercomputer Center in Tianjin (NSCC-TJ) for providing computer time.

References

1. M. P. Martín, *J. Fluid Mech.* **570**, 347 (2007).
2. Y. Guo and N. A. Adams, Numerical investigation of supersonic turbulent boundary layers with high wall temperature, *Proc. Summer Program of the Center for Turbulence Research* (Stanford University, 1994).
3. S. E. Guarini *et al.*, *J. Fluid Mech.* **414**, 1 (2000).
4. M. Rai, T. Gatski and G. Erlebacher, Direct simulation of spatially evolving compressible turbulent boundary layers, *33rd Aerospace Sciences Meeting and Exhibit* (1995).
5. E. R. Van Driest, *J. Aero. Sci.* **18**, 3 (1951).
6. S. Pirozzoli, F. Grasso and T. B. Gatski, *Phys. Fluids* **16**(3), 530 (2004).
7. H. Gao *et al.*, *Chin. Phys. Lett.* **22**, 1709 (2005).
8. T. Maeder, N. A. Adams and L. Kleiser, *J. Fluid Mech.* **429**, 187 (2001).
9. X. L. Li, D. X. Fu and Y. W. Ma, *Chin. Phys. Lett.* **23**, 1519 (2006).
10. L. Duan, I. Beekman and M. P. Martín, *J. Fluid Mech.* **655**, 419 (2010).
11. L. Duan, I. Beekman and M. P. Martín, *J. Fluid Mech.* **672**, 245 (2011).
12. L. Duan and M. P. Martín, *J. Fluid Mech.* **684**, 25 (2011).
13. A. Walz, *Boundary Layers of Flow and Temperature* (MIT Press, 1969).
14. P. G. Huang, G. N. Colemann and P. Bradshaw, *J. Fluid Mech.* **305**, 158 (1995).
15. M. Lagha *et al.*, *Phys. Fluids* **23**, 015106 (2011).
16. M. Lagha *et al.*, Near-wall dynamics of compressible boundary layers, *Phys. Fluids* **23**, 065109 (2011).
17. X. Liang *et al.*, DNS and analysis of a spatially evolving hypersonic turbulent boundary layer over a flat plate at Mach 8, *Sci. Sin. Phys. Mech. Astron.* **42**, 282 (2012).
18. X. Liang and X. L. Li, Direct numerical simulation on Mach number and wall temperature effects in the turbulent flows of flat-plate boundary layer, *Commun. Comput. Phys.* **17**, 189 (2015).

19. L. Duan, M. M. Choudhari and C. Zhang, Pressure fluctuations induced by a hypersonic turbulent boundary layer, *J. Fluid Mech.* **804**, 578 (2016).
20. C. Zhang, L. Duan and M. M. Choudhari, Effect of wall cooling on boundary-layer-induced pressure fluctuations at Mach 6, *J. Fluid Mech.* **822**, 5 (2017).
21. X. Li, C. P. Yu and X. L. Li, Wall temperature effects on the Reynold stress of flat-plate turbulent boundary layer: A numerical investigation, *Adv. Appl. Math. Mech.* **11**, 653 (2019).
22. X. Li *et al.*, Statistical analysis of temperature distribution on vortex surfaces in hypersonic turbulent boundary layer, *Phys. Fluids* **31**, 106101 (2019).
23. A. J. Smits and J. P. Dussuage, *Turbulent Shear Layers in Supersonic Flow* (Springer, 1996).
24. X. Li *et al.*, Correlation between density and temperature fluctuations of hypersonic turbulent boundary layers at $Ma_\infty = 8$, *AIP Adv.* **10**, 075101 (2020).
25. A. J. Smits and K. C. Muck, Experimental study of three shock wave/turbulent boundary layer interactions, *J. Fluid Mech.* **182**, 291 (1987).
26. A. Talamelli, A. Segalini, R. Örlü *et al.*, Correcting hot-wire spatial resolution effects in third- and fourth-order velocity moments in wall-bounded turbulence, *Exp. Fluids* **54**, 1496 (2013).
27. A. Trettel and J. Larsson, Mean velocity scaling for compressible wall turbulence with heat transfer, *Phys. Fluids* **28**, 026102 (2016).
28. C. Brun, M. P. Boiarciuc, M. Haberkorn *et al.*, Large eddy simulation of compressible channel flow, *Theor. Comput. Fluid Dyn.* **22**, 189 (2008).
29. C. Q. Liu, Y. Q. Wang, Y. D. Yang *et al.*, New omega vortex identification method, *Sci. China Phys. Mech. Astron.* **59**, 684711 (2016).
30. C. Q. Liu and Y. Q. Wang, *Liutex and Third Generation of Vortex Definition and Identification for Turbulence Research* (Springer Press, 2021).
31. S. Pirozzoli, M. Bernardini and F. Grasso, Characterization of coherent vortical structures in a supersonic turbulent boundary layer, *J. Fluid Mech.* **613**, 205 (2011).
32. Y. B. Chu, Y. Q. Zhuang and X. Y. Lu, Effect of wall temperature on hypersonic turbulent boundary layer, *J. Turbulence* **14**, 37 (2013).
33. J. R. Hearst *et al.*, Uniform momentum zones in a turbulent boundary layer subjected to freestream turbulence, *J. Fluid Mec*h. **915**, A109 (2021).
34. M. Bross, S. Scharnowski and C. Kähler, Large-scale coherent structures in compressible turbulent boundary layers, *J. Fluid Mech.* **911**, A2 (2021).